Alamouti Coding for DFT Spreading-based Low PAPR FBMC

Kwonhue Choi

***Abstract*—Thus far, the solutions for the two major issues of FBMC/OQAM (filter bank multicarrier with offset quadrature amplitude modulation), i.e., 1) high PAPR and 2) incompatibility with MIMO have been devised exclusive of each other and thus, the signal formats and processings are also exclusive. Therefore, how to constructively combine their solutions in a single system is another challenging issue. As a specific solution to this, we extend the idea of DFT spreading-based Low PAPR FBMC scheme to the ICI-free Alamouti-coded FBMC. In order to inherit the merits of the two schemes, we first provide the required modifications for combining the two schemes. A mathematical analysis confirms that even with frequency reversal Alamouti code arrangement and subblock partitioning, the proposed scheme still achieves the single carrier effect of DFT spreading. The simulation results reveal that the proposed scheme achieves substantially lower PAPR than the previous Alamouti-coded FBMC scheme. Moreover, owing to the additional frequency diversity via DFT spreading, the proposed scheme with properly chosen subblock size achieves even lower BER than the theoretical Alamouti-coded BER with a diversity order of two. Considering the PAPR, BER, and data rate loss, we conclude that the proposed scheme is a competitive solution for Alamouti-coded multicarrier system.**

***Index Terms*—FBMC (filter bank multicarrier), Alamouti code, PAPR (peak to average power ratio), Offset QAM (OQAM), MIMO (multiple-input multiple-output)**

I. Introduction

Although FBMC-OQAM (filter bank multicarrier with offset quadrature amplitude modulation) has a significant number of merits, there are still some issues that need to be resolved. For instance, as FBMC[1] is based on multicarrier modulation, it has a high PAPR (peak to average power ratio) as OFDM (orthogonal frequency division multiplexing) does. The practical high power amplifier in the transmitter has a limited linear range. Hence, in case of high amplification gain, a high PAPR could cause signal clipping or other nonlinearities in the FBMC signal [1–3]. Various schemes to reduce the PAPR of FBMC were proposed in [4–10], but there exist some practical issues, such as considerable side information overhead, high computational complexity and data rate loss [5, 10]. Recently, in order to overcome these practical issues, a new type of FBMC called *Low PAPR FBMC* (LP-FBMC in short) was proposed in [11]. Basically, LP-FBMC employs DFT (discrete Fourier transform) spreading and candidate selection. Unlike the conventional DFT-spread FBMC [12, 13], the phase shift terms of FBMC signal format are set to meet a special condition called ITSM (identically time-shifted multicarrier) condition to fully utilize the single carrier effect of DFT spreading. With a fractional complexity overhead compared with the previous DFT-spread FBMC, LP-FBMC achieves a PAPR reduction comparable to that of DFT-spread OFDM (DFT-S-OFDM or SC-FDMA). In addition, LP-FBMC requires very small side information (two bits per subframe) compared to the other typical PAPR reduction schemes such as PTS (partial transmit sequence) and SLM (selective mapping).

Along with high PAPR, another issue of FBMC is the difficulty to combine it with Alamouti code, due to the intrinsic inter-carrier interference in the complex domain [14, 15]. Recently, just a few studies have been made to overcome this issue in [15–18] by different approaches whereas there exist considerable studies on the combination of FBMC and MIMO (spatial multiplexing) techniques including [16, 19–21]. Moreover, Alamouti-coded FBMC schemes in [15–17] require the considerable computation complexities in the transmitter or the receiver side and another Alamouti-coded FBMC scheme in [18] has a loss in spectral efficiency due to cyclic prefix. In [22], a simple block Alamouti-coded scheme was proposed for FBMC. This scheme is based on the assumption of static fading over the block, and therefore this scheme undergoes severe degradation as the Doppler rate increases. In addition, due to its time reversal (TR) block structure, decoding latency is inevitable. In [23–25], a FRAC (frequency reversal Alamouti-coded) scheme for FBMC is proposed, which we call FRAC-FBMC in this paper. By arranging the Alamouti-coded symbol in a frequency reversal manner and simply setting the phase shift terms for the frequency reversal counter part to satisfy Hermitian symmetry, the intrinsic inter-antenna ICI (inter-carrier interference) terms are self cancelled in the typical Alamouti decoding stage. Hence, FRAC-FBMC achieves near ICI-free performance with very simple signal modifications and negligible computation complexity compared to the existing Alamouti-coded FBMC schemes. In addition, FRAC-FBMC has negligible decoding latency because the Alamouti-coded symbol pairs belong to the same FBMC symbol unlike [22]. The signal structure proposed in [23] has been further improved in [25] by removing the need for null insertion into the center subcarrier.

As we have reviewed, there exist some researches on the PAPR reduction scheme for FBMC and on applying the MIMO scheme to FBMC. However, these two issues have been addressed rather recently, and therefore the researches on these two issues have been performed exclusively. These

This research was supported in part by Basic Science Research Program through the National Research Foundation (NRF) (2018R1D1A3A03000837) funded by the Ministry of Education, Korea, and the MSIT(Ministry of Science and ICT), Korea, under the ITRC(Information Technology Research Center) support program(IITP-2018-2016-0-00313) supervised by the IITP(Institute for Information & communications Technology Promotion).

K. Choi is with the Department of Information and Communication Engineering, Yeungnam University, Korea. e-mail: gonew@yu.ac.kr, Tel: +82-53-810-3516

[1]Hereinafter, FBMC-OQAM is referred to as FBMC for simplicity.

two issues are very crucial in the current and next generation wireless communication systems. Therefore, it is very essential to tackle these two issues together in the same system in a timely manner. To this end, in this paper, we extend the LP-FBMC scheme in [11] to the case employing transmit spatial diversity. As a target MIMO technique, we select Alamouti code as in [22, 23, 25]. Specifically, we apply the idea of LP-FBMC to FRAC-FBMC proposed in [25]. In the context of DFT-S-OFDM, a PAPR preserving Alamouti-type code has been proposed in [26]; however, it cannot be employed to FBMC, which is inherently incompatible with Alamouti code and has a negligible single carrier effect of DFT spreading unlike DFT-S-OFDM.

For combining the two schemes, i.e., LP-FBMC and FRAC-FBMC, we need to overcome some challenging issues. For instance, it is obvious that we cannot perform LP-FBMC technique on Alamouti-coded symbols because DFT spreading in LP-FBMC breaks Alamouti code structure. Reversely, if we directly perform Alamouti coding on the channel symbols of LP-FBMC, i.e., the DFT-spread data symbols with ITSM condition [11], then, ITSM condition is not maintained and thus, the single carrier effect diminishes. This problem is not limited to combining LP-FBMC and FRAC-FBMC but to combining the other PAPR reduction schemes (such as PTS and SLM) for FBMC and Alamouti coding because the Alamouti code structure and the PAPR-reduced signal structure break each other. Therefore, we need to come up with a judiciously unified transmitter structure, which maintains the key design requirements such as basic FBMC signal format, frequency reversal Alamouti code structure [25], and ITSM-conditioned DFT spreading [11]. Most importantly, even though we can find a unified structure satisfying all these signal design requirements, we need to modify the structure further in order to fully inherit the merits of the two schemes, i.e., low PAPR and inter-antenna ICI-free Alamouti coding. The major contribution of our work is in resolving these issues. In addition, we mathematically confirm that even with the frequency reversal Alamouti code arrangement and subblock partitioning, the proposed scheme still achieves single carrier effect of DFT spreading. We intensively investigate and compare the PAPR, BER, and data rate loss with those of the previous scheme and show that the proposed scheme is a competitive solution for Alamouti-coded FBMC systems.

The remainder of this paper is structured as follows: In Section II, the FRAC-FBMC and LP-FBMC schemes are reviewed. In Section III-A, for a preliminary study, we first check the validity of combining LP-FBMC and FRAC symbol arrangement. In Section III-B and Section III-C, we investigate and provide the required modifications for combining the two schemes and in Section III-D, the low complexity implementation of the transmitter is provided. In Section III-E, the subblock partitioning idea to cope with frequency selectivity is explained. In Section IV, we prove that the signal of the proposed scheme takes the single carrier form. In Section V, the complexity of the proposed scheme is calculated and in Section VI, the performance of the proposed scheme is assessed in terms of PAPR, BER, and data rate loss. In Section VII, the overall comparison among the various Alamouti-coded multicarrier schemes is given. Finally, the conclusions are made in Section VIII.

The following notations are used in this paper.

- $\Re\{x\}$ and $\Im\{x\}$ denote the real and imaginary parts of a complex number x, respectively,
- $x_{a:b}$ denotes a partition of a vector $\mathbf{x}$, i.e., $[x_a, x_{a+1}, x_{a+2}, \cdots, x_b]$,
- $\overleftarrow{\mathbf{x}}$ denotes the reversely ordered version of a vector $\mathbf{x}$. That is, for a vector $\mathbf{x}$ of length N denoted by $[x_0, x_1, x_2, \cdots, x_{N-1}]$, $\overleftarrow{\mathbf{x}} = [x_{N-1}, x_{N-2}, x_{N-3}, \cdots, x_0]$. Thus, for a partitioned vector denoted above, $\overleftarrow{x_{a:b}} = [x_b, x_{b-1}, x_{b-2}, \cdots, x_a]$,
- $[\mathbf{x}, \mathbf{y}]$ denotes the concatenated vector of the vectors $\mathbf{x}$ and $\mathbf{y}$. If $\mathbf{x}$ and $\mathbf{y}$ are column vectors, $[\mathbf{x}, \mathbf{y}]$ denotes a vertical concatenation and thus $[\mathbf{x}, \mathbf{y}]$ is also a column vector.

The simulation code for the proposed scheme is downloadable at http://bwc.yu.ac.kr/download.html

II. Reviews on FRAC-FBMC and LP-FBMC

To help understand the proposed scheme, which combines FRAC-FBMC and LP-FBMC, the following subsections first review how the waveforms are generated in each scheme.

A. FRAC-FBMC

Denote the number of subcarriers by N and the number of complex data symbols per subcarrier in a data frame by M. Then, consider a data frame consists of N by M complex data symbols, where $d_{x,y}$ denotes the (x, y)-th complex data symbol element. The FBMC signal is generally expressed as follows:

$$s(t) = \sum_{n=0}^{N-1} \sum_{k=0}^{2M-1} c_{n,k} \zeta_{n,k} p(t - kT/2) e^{j\frac{2\pi nt}{T}} \tag{1}$$

where n denotes subcarrier index, k denotes symbol index in time axis, T denotes FBMC symbol duration and $p(t)$ is the FBMC prototype pulse for spectrum localization such as PHYDYAS pulse or IOTA pulse. The term $c_{n,k}$ denotes a real symbol transmitted on the nth subcarrier at $t = kT/2$. In the conventional FBMC, $c_{n,k}$ is simply set as follows:

$$c_{n,k} = \begin{cases} \Re\{d_{n,m}\} & \text{if } k = 2m \\ \Im\{d_{n,m}\} & \text{if } k = 2m+1. \end{cases} \tag{2}$$

The phase shift pattern $\zeta_{n,k}$ must satisfy the following rule,

$$\zeta_{n,k} = \begin{cases} 1 \text{ (or } -1) & \text{if } n+k = \text{even}, \\ j \text{ (or } -j) & \text{if } n+k = \text{odd}, \end{cases} \tag{3}$$

which is the basic requirement for FBMC signal form [14, 23].

In FRAC-FBMC, each of the data column vectors $d_{0:(N-1),0}$, $d_{0:(N-1),1}$, $d_{0:(N-1),2}$, $\cdots$ is split into two half column vectors, i.e., $d_{0:(N/2-1),m}$ and $d_{(N/2):(N-1),m}$ for two transmit antennas [25]. Let us express $d_{n,m} = X^{(A)}_{n,m} + jY^{(A)}_{n,m}$ and $d_{N/2+n,m} = X^{(B)}_{n,m} + jY^{(B)}_{n,m}$. Then, the FRAC symbol arrangement is performed prior to FBMC modulation as shown in Fig. 1, where $c^{(A)}_{n,k}$ and $c^{(B)}_{n,k}$ on the top of the tables correspond to $c_{n,k}$ in (1) transmitted by Antennas A and B, respectively. Note that in Fig. 1, $c^{(A)}_{n,k}$ and $c^{(B)}_{n,k}$ in the second half subcarriers are Alamouti code pairs

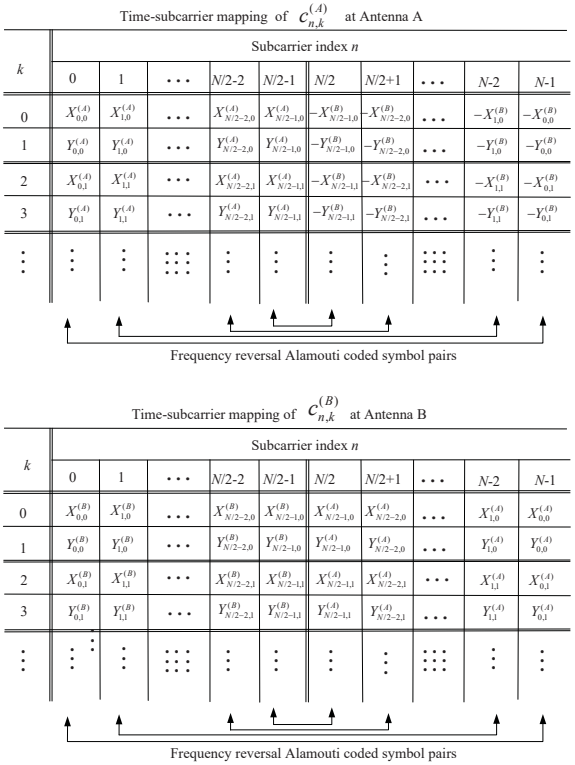

Fig. 1. Frequency reversal Alamouti-coded symbol arrangement prior to FBMC modulation.

(arranged in a frequency reversal manner) of the counter part in the first half subcarriers.

Let $\zeta_{n,k}^{(A)}$ and $\zeta_{n,k}^{(B)}$ denote $\zeta_{n,k}$ for Antennas A and B, respectively. On top of the FRAC symbol arrangement, the second half parts of $\zeta_{n,k}^{(A)}$ and $\zeta_{n,k}^{(B)}$ are set to satisfy the χ-multiplied Hermitian symmetry to the first half parts of $\zeta_{n,k}^{(B)}$ and $\zeta_{n,k}^{(A)}$, respectively, as follows:

$$\zeta_{n,k}^{(A)} = \chi\zeta_{N-n-1,k}^{*(B)} \text{ for } N/2 \le n \le N-1, \quad (4)$$

$$\zeta_{n,k}^{(B)} = \chi\zeta_{N-n-1,k}^{*(A)} \text{ for } N/2 \le n \le N-1 \quad (5)$$

where χ = j (or -j). This rule was devised in [25] for the self ICI cancellation of frequency reversal Alamouti code in the case of no null insertion to the center subcarrier. For the received signal model and demodulation process, the readers can refer to the related equations in [23, 25][2]. Also, details on how the inter-antenna ICI is self cancelled in FRAC-FBMC given in [23, 25] are skipped as they are out of the scope of this study.

B. LP-FBMC

To maximize the single carrier effect of DFT spreading, a special condition of the coefficients at each subcarrier's in-phase and quadrature-phase (IQ) channels called ITSM condition should be satisfied. Based on this condition, LP-FBMC is proposed in [11]. Also in LP-FBMC, for further PAPR reduction, the four candidate versions of the DFT-spread and ITSM-conditioned FBMC waveform are generated and then, the one with minimum peak power is selected. The PAPR and BER simulation code for LP-FBMC is downloadable from a public website [27]. Fig. 2 shows the structure of an LP-FBMC transmitter [11]. The input $d_{(0:N_D-1),m}$ denotes the mth complex data vector of size N_D. The IDFT (inverse discrete Fourier transform)-PPN (poly-phased network) technique is employed for the pulse shaped multicarrier modulation part. Specifically, the PPN is implemented by using expanding-and-add operation[3] which is graphically illustrated in [11]. The shaded parts indicate the additional blocks to the conventional FBMC transmitter.

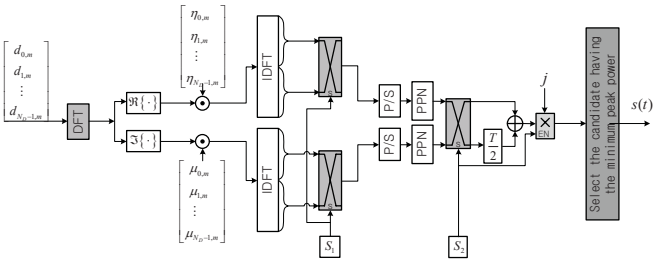

Fig. 2. Structure of LP-FBMC transmitter.

The main distinguishable features from the conventional FBMC are as follows.

- The DFT spreading is performed on the input prior to the FBMC modulation stage.
- The phase shift term η and μ should satisfy the following condition (called ITSM condition) to fully exploit the single carrier effect of DFT spreading [11].

$$(\eta_{n,m}, \mu_{n,m}) = (j^n, \quad j(-j)^n) \text{ or,} \quad (6)$$

$$(\eta_{n,m}, \mu_{n,m}) = \left((-j)^n, \quad j^{n+1}\right). \quad (7)$$

  Note that the term $(-1)^m$ in the equations in ((3),(15)) and ((18), (19)) in [11] is detached in (6) and (7) because it is not mandatory for the FBMC signal format [23, 25] or the ITSM condition and it simply toggles the signs of the consecutive FBMC symbols.
- The four ITSM-conditioned candidate signals are generated by setting two switching control bits (S_1, S_2) to (0,0), (0,1), (1,0) and (1,1). In the final stage, the candidate with the minimum peak is selected to be transmitted.

III. Combining LP-FBMC and FRAC-FBMC

A. Validity of combining

In the proposed scheme, we follow the symbol arrangement of the frequency reversal Alamouti code (FRAC), as shown in Fig. 1. Combining the idea of LP-FBMC with the FRAC-FBMC scheme, the proposed scheme has two main differences from FRAC-FBMC. Firstly, the two half data vectors

[2]We follow the notations in [11], which is the most recent reference. Therefore, the readers attention should be paid for referring to [23, 25] because some notations used in [23, 25] are different from those in this paper, such as the subcarrier index, the symbol index and the index ranges.

[3]On the other hand, in the receiver side, the PPN employs folding-and-accumulation operation for matched filtering [27, 28].

$d_{0:(N/2-1),m}$ and $d_{N/2:(N-1),m}$ go through DFT separately prior to the FRAC symbol arrangement, as shown in the input stage of Fig. 3 in Section III-B. Secondly, in addition to the rule in (4) and (5), by which $\zeta_{n,k}^{(A)}$ and $\zeta_{n,k}^{(B)}$ in the second half subcarriers are determined according to those in the first half subcarriers, we further restrict $\zeta_{n,k}^{(A)}$ and $\zeta_{n,k}^{(B)}$ in the first half subcarriers so that the first half subcarrier part satisfies the so called ITSM (identically time shifted multicarrier) condition to fully exploit the single carrier effect of DFT spreading [11]. Prior to finding the solution for this restriction in the next subsection, we encounter an important question : *By this restriction, can we get the single carrier effect in the second half subcarrier part as well?* We cannot separately design the second half subcarrier part because the symbols and phase terms are all determined by the frequency reversal arrangement. Hence, this question should be answered before we further develop the idea of combining LP-FBMC and FRAC-FBMC.

To do this, we need to first find the mathematical expressions for the waveforms in the first and second half subcarrier parts. Substituting the elements of the mapping tables for $c_{n,k}^{(A)}$ and $c_{n,k}^{(B)}$ in Fig. 1 into (1), the transmit signal from Antenna A $s^{(A)}(t)$ and the transmit signal from Antenna B $s^{(B)}(t)$ are written as:

$$\begin{aligned} s^{(A)}(t) = &\sum_{n=0}^{\frac{N}{2}-1}\sum_{m=0}^{M-1} X_{n,m}^{(A)}\zeta_{n,2m}^{(A)} p(t-mT)e^{j\frac{2\pi nt}{T}} \\ &- \sum_{n=\frac{N}{2}}^{N-1}\sum_{m=0}^{M-1} X_{N-n-1,m}^{(B)}\zeta_{n,2m}^{(A)} p(t-mT)e^{j\frac{2\pi nt}{T}} \\ &+ \sum_{n=0}^{\frac{N}{2}-1}\sum_{m=0}^{M-1} Y_{n,m}^{(A)}\zeta_{n,2m+1}^{(A)} p\left(t-mT-\tfrac{T}{2}\right) e^{j\frac{2\pi nt}{T}} \\ &- \sum_{n=\frac{N}{2}}^{N-1}\sum_{m=0}^{M-1} Y_{N-n-1,m}^{(B)}\zeta_{n,2m+1}^{(A)} p\left(t-mT-\tfrac{T}{2}\right) e^{j\frac{2\pi nt}{T}} \quad (8) \end{aligned}$$

$$\begin{aligned} s^{(B)}(t) = &\sum_{n=0}^{\frac{N}{2}-1}\sum_{m=0}^{M-1} X_{n,m}^{(B)}\zeta_{n,2m}^{(B)} p(t-mT)e^{j\frac{2\pi nt}{T}} \\ &+ \sum_{n=\frac{N}{2}}^{N-1}\sum_{m=0}^{M-1} X_{N-n-1,m}^{(A)}\zeta_{n,2m}^{(B)} p(t-mT)e^{j\frac{2\pi nt}{T}} \\ &+ \sum_{n=0}^{\frac{N}{2}-1}\sum_{m=0}^{M-1} Y_{n,m}^{(B)}\zeta_{n,2m+1}^{(B)} p\left(t-mT-\tfrac{T}{2}\right) e^{j\frac{2\pi nt}{T}} \\ &+ \sum_{n=\frac{N}{2}}^{N-1}\sum_{m=0}^{M-1} Y_{N-n-1,m}^{(A)}\zeta_{n,2m+1}^{(B)} p\left(t-mT-\tfrac{T}{2}\right) e^{j\frac{2\pi nt}{T}}. \quad (9) \end{aligned}$$

It should be noted that we are considering the case when the DFT spread data symbols are mapped in the input frame for FRAC in Fig. 1. Hence, in (8) and (9), $X_{0:N/2-1,m}^{(A)}$ and $Y_{0:N/2-1,m}^{(A)}$ denote the real and imaginary parts of the DFT outputs of the first half data symbol vector $d_{0:N/2-1,m}$ and, $X_{0:N/2-1,m}^{(B)}$ and $Y_{0:N/2-1,m}^{(B)}$ denote the real and imaginary parts of the DFT outputs of the second half data symbol vector $d_{N/2:N-1,m}$, as shown in Fig. 3. The first two double summation terms in (8) and (9) correspond to the on-time FBMC signal, which carries the symbols in the even rows of the time-frequency matrices shown in Fig. 1. On the other hand, the latter two double summation terms correspond to the $T/2$-delayed FBMC signal which carries the symbols in the odd rows. Thus, the $T/2$-spaced FBMC symbol index k in $\zeta_{n,k}^{(A)}$ and $\zeta_{n,k}^{(B)}$ are set to $2m$ and $2m+1$ in the first and the latter two summations in (8) and (9), respectively.

Mentioning first the derivation in Section IV, the proposed FBMC waveform can be represented by a single carrier form of very narrow pulse train and the pulse width is much smaller than the width of the shaping pulse $p(t)$ (See Fig. 8). This allows us to assume that the shaping pulse $p(t)$ is constant over the quite large number of consecutive narrow pulses in single carrier form expression. Therefore, let us temporarily ignore pulse shaping and limit to the $2m$-th and $2m+1$-th FBMC symbols, which carry the real and imaginary parts of the m-th DFT-spread complex data symbol vector, respectively. Then, grouping the left and the second half subcarrier parts of (8) and (9), $s^{(A)}(t)$ and $s^{(B)}(t)$ are written as follows:

$$\begin{aligned} s^{(A)}(t) = &\sum_{n=0}^{N/2-1}\left\{X_{n,m}^{(A)}\zeta_{n,2m}^{(A)} + Y_{n,m}^{(A)}\zeta_{n,2m+1}^{(A)}\right\} e^{j\frac{2\pi nt}{T}} \\ &+ \sum_{n=N/2}^{N-1}(-1)\left\{X_{N-n-1,m}^{(B)}\zeta_{n,2m}^{(A)} + Y_{N-n-1,m}^{(B)}\zeta_{n,2m+1}^{(A)}\right\} e^{j\frac{2\pi nt}{T}} \quad (10) \end{aligned}$$

$$\begin{aligned} s^{(B)}(t) = &\sum_{n=0}^{N/2-1}\left\{X_{n,m}^{(B)}\zeta_{n,2m}^{(B)} + Y_{n,m}^{(B)}\zeta_{n,2m+1}^{(B)}\right\} e^{j\frac{2\pi nt}{T}} \\ &+ \sum_{n=N/2}^{N-1}\left\{X_{N-n-1,m}^{(A)}\zeta_{n,2m}^{(B)} + Y_{N-n-1,m}^{(A)}\zeta_{n,2m+1}^{(B)}\right\} e^{j\frac{2\pi nt}{T}}. \quad (11) \end{aligned}$$

The first and the second summations in each equation correspond to the first and the second half subcarrier signals, respectively. By using (4), (5) and the fact that $X_{n,m}$ and $Y_{n,m}$ are real-valued, the second half subcarrier signal of Antenna A in (10) is rewritten as follows:

$$\begin{aligned} &\sum_{n=N/2}^{N-1}(-1)\left\{X_{N-n-1,m}^{(B)}\chi\zeta_{N-n-1,2m}^{(B)*} + Y_{N-n-1,m}^{(B)}\chi\zeta_{N-n-1,2m+1}^{(B)*}\right\} e^{j\frac{2\pi nt}{T}} \\ &= -\chi e^{j\frac{2\pi(N-1)t}{T}}\sum_{n=0}^{N/2-1}\left\{X_{n,m}^{(B)}\zeta_{n,2m}^{(B)*} + Y_{n,m}^{(B)}\zeta_{n,2m+1}^{(B)*}\right\} e^{j\frac{-2\pi nt}{T}} \\ &= -\chi e^{j\frac{2\pi(N-1)t}{T}}\left[\sum_{n=0}^{N/2-1}\left\{X_{n,m}^{(B)}\zeta_{n,2m}^{(B)} + Y_{n,m}^{(B)}\zeta_{n,2m+1}^{(B)}\right\} e^{j\frac{2\pi nt}{T}}\right]^* \quad (12) \end{aligned}$$

Note that the last summation is equal to the first half subcarrier signal of Antenna B in (11). Similarly, we can write the second half subcarrier signal of Antenna B (= the second summation in (11)) as $\chi e^{j\frac{2\pi(N-1)t}{T}}\left[\sum_{n=0}^{N/2-1}\left\{X_{n,m}^{(A)}\zeta_{n,2m}^{(A)} + Y_{n,m}^{(A)}\zeta_{n,2m+1}^{(A)}\right\} e^{j\frac{2\pi nt}{T}}\right]^*$ where the summation term is equal to the first half subcarrier signal of Antenna A in (10). Meanwhile, the first half subcarrier signals of Antennas A and B will be restricted to be the single carrier signals by the ITSM condition in Section III-C. As the conjugate operation results in frequency reversal spectrum and the multiplication of the complex sinusoid term $e^{j\frac{2\pi(N-1)t}{T}}$

does not change the spectrum shape, we confirm that in the proposed signal structure, the second half subcarrier signals of Antennas A and B are also single carrier signals as long as the first half subcarrier signals are single carrier signals.

B. IDFT-PPN-based transmitter structure

By using an IDFT-PPN-based structure, as shown in Fig. 2, we can generate $s^{(A)}(t)$ in (8) and $s^{(B)}(t)$ in (9). For the ease of explanation, let us show the completed solution in Fig. 3 first and then explain how to get this.

The first two double summation terms in (8) (or (9)) correspond to the preceding part of the OQAM symbols, and are generated by the first and third (to the top) IDFT-PPN branches in Fig. 3. The latter two double summation terms in (8) (or (9)) correspond to the $T/2$-delayed part of OQAM symbols, and are generated by the second and fourth IDFT-PPN branches. Note that the latter two double summation terms in (8) (or (9)) are not IDFT-PPN structure-equivalent forms. This is because, in the IDFT-PPN structure, the $T/2$ delay for OQAM is introduced necessarily *after* the multicarrier modulation as shown in the second and fourth IDFT-PPN branches in Fig. 3, whereas in (8) and (9), the delay is introduced *prior* to multicarrier modulation. Hence, we have to change those into IDFT-PPN structure-equivalent forms. By changing $e^{j\frac{2\pi nt}{T}}$ into $(-1)^n e^{j\frac{2\pi n(t-T/2)}{T}}$ in the latter two double summations in (8), we first rewrite the equation $s^{(A)}(t)$ so that the muticarrier terms for the $T/2$-delayed symbols also appear as $T/2$-delayed as follows:

$$\begin{aligned} s^{(A)}(t) = & \sum_{n=0}^{N/2-1}\sum_{m=0}^{M-1} X^{(A)}_{n,m}\zeta^{(A)}_{n,2m}p\left(t-mT\right)e^{j\frac{2\pi nt}{T}} \\ & + \sum_{n=N/2}^{N-1}\sum_{m=0}^{M-1}\left(-X^{(B)}_{N-n-1,m}\right)\zeta^{(A)}_{n,2m}p\left(t-mT\right)e^{j\frac{2\pi nt}{T}} \\ & + \sum_{n=0}^{N/2-1}\sum_{m=0}^{M-1} Y^{(A)}_{n,m}(-1)^n\zeta^{(A)}_{n,2m+1}p\left(t-mT-\tfrac{T}{2}\right)e^{j\frac{2\pi n(t-T/2)}{T}} \\ & + \sum_{n=N/2}^{N-1}\sum_{m=0}^{M-1}\left(-Y^{(B)}_{N-n-1,m}\right)(-1)^n\zeta^{(A)}_{n,2m+1}p\left(t-mT-\tfrac{T}{2}\right)e^{j\frac{2\pi n(t-T/2)}{T}}. \end{aligned} \tag{13}$$

Let $\mathbf{i}^{(A)}_{OnTime}$ denote the input to the first (to the top) IDFT in Fig. 3 for generating the first two double summation terms in (13). Then, we can set up $\mathbf{i}^{(A)}_{OnTime}$ by extracting the phase shifted (ζ-multiplied) symbol terms (in between $\sum_{m=0}^{M-1}$ and $p(t-mT)$) and then lining them up in the subcarrier axis as follows:

$$\mathbf{i}^{(A)}_{OnTime} = \left[X^{(A)}_{\left(0:\frac{N}{2}-1\right),m}\odot\zeta^{(A)}_{\left(0:\frac{N}{2}-1\right),2m}, \overleftarrow{-X^{(B)}_{\left(0:\frac{N}{2}-1\right),m}}\odot\zeta^{(A)}_{\left(\frac{N}{2}:(N-1)\right),2m}\right], \tag{14}$$

where $\odot$ denotes element-by-element multiplication. By the condition in (4), we have

$$\begin{aligned} \mathbf{i}^{(A)}_{OnTime} &= \left[X^{(A)}_{\left(0:\frac{N}{2}-1\right),m}\odot\zeta^{(A)}_{\left(0:\frac{N}{2}-1\right),2m}, \overleftarrow{-X^{(B)}_{\left(0:\frac{N}{2}-1\right),m}}\odot\chi\overleftarrow{\zeta^{(B)*}_{\left(0:\frac{N}{2}-1\right),2m}}\right] \\ &= \left[X^{(A)}_{\left(0:\frac{N}{2}-1\right),m}\odot\zeta^{(A)}_{\left(0:\frac{N}{2}-1\right),2m}, -\chi\overleftarrow{\left(X^{(B)}_{\left(0:\frac{N}{2}-1\right),m}\odot\zeta^{(B)}_{\left(0:\frac{N}{2}-1\right),2m}\right)^*}\right] \end{aligned} \tag{15}$$

If we denote the second IDFT input in Fig. 3 for generating the latter two double summation terms in (13) as $\mathbf{i}^{(A)}_{Delayed}$, and use the condition in (4), we have

$$\begin{aligned} \mathbf{i}^{(A)}_{Delayed} = & \left[Y^{(A)}_{\left(0:\frac{N}{2}-1\right),m}\odot\zeta^{(A)}_{\left(0:\frac{N}{2}-1\right),2m+1}, -\chi\overleftarrow{\left(Y^{(B)}_{\left(0:\frac{N}{2}-1\right),m}\odot\zeta^{(B)}_{\left(0:\frac{N}{2}-1\right),2m+1}\right)^*}\right] \\ & \odot[1,-1,1-1,\cdots,-1] \end{aligned} \tag{16}$$

where we additionally have the sign toggle vector $[1,-1,1-1,\cdots-1]$ due to the term $(-1)^n$ in (13) for the IDFT-PPN equivalent form. Similarly, if we denote the third and fourth IDFT inputs for generating the on-time and $T/2$-delayed terms in (9) as $\mathbf{i}^{(B)}_{OnTime}$ and $\mathbf{i}^{(B)}_{Delayed}$, respectively, then we have,

$$\mathbf{i}^{(B)}_{OnTime} = \left[X^{(B)}_{\left(0:\frac{N}{2}-1\right),m}\odot\zeta^{(B)}_{\left(0:\frac{N}{2}-1\right),2m}, \chi\overleftarrow{\left(X^{(A)}_{\left(0:\frac{N}{2}-1\right),m}\odot\zeta^{(A)}_{\left(0:\frac{N}{2}-1\right),2m}\right)^*}\right] \tag{17}$$

$$\begin{aligned} \mathbf{i}^{(B)}_{Delayed} = & \left[Y^{(B)}_{\left(0:\frac{N}{2}-1\right),m}\odot\zeta^{(B)}_{\left(0:\frac{N}{2}-1\right),2m+1}, \chi\overleftarrow{\left(Y^{(A)}_{\left(0:\frac{N}{2}-1\right),m}\odot\zeta^{(A)}_{\left(0:\frac{N}{2}-1\right),2m+1}\right)^*}\right] \\ & \odot[1,-1,1-1,\cdots,-1]. \end{aligned} \tag{18}$$

Comparing (15) and (17), note that the following hold:

$$\text{second half of } \mathbf{i}^{(A)}_{OnTime} = -\chi\overleftarrow{\left(\text{first half of } \mathbf{i}^{(B)}_{OnTime}\right)^*} \tag{19}$$

$$\text{second half of } \mathbf{i}^{(B)}_{OnTime} = \chi\overleftarrow{\left(\text{first half of } \mathbf{i}^{(A)}_{OnTime}\right)^*}. \tag{20}$$

By neglecting the term $[1,-1,1-1,\cdots,-1]$ in (16) and (18), we have

$$\text{second half of } \mathbf{i}^{(A)}_{Delayed} = -\chi\overleftarrow{\left(\text{first half of } \mathbf{i}^{(B)}_{Delayed}\right)^*} \tag{21}$$

$$\text{second half of } \mathbf{i}^{(B)}_{Delayed} = \chi\overleftarrow{\left(\text{first half of } \mathbf{i}^{(A)}_{Delayed}\right)^*}. \tag{22}$$

Using these frequency reversal symmetric rules between the two antennas, the transmit signals $s^{(A)}(t)$ and $s^{(B)}(t)$ can be finally generated in the IDFT-PPN structure as shown in Fig 3. It should be noted that the signal vectors are expressed in the column vector form for ease of presentation, and therefore the reversely ordered vector operation is denoted by the vertical arrows $\uparrow\downarrow$. Note that the terms $[1,-1,1-1,\cdots,-1]$ in (16) and (18) (that have been temporarily neglected in (21) and (22)) are implemented right before the IDFTs for $T/2$-delayed branches of the two antenna signals.

C. ITSM-conditioned waveform candidate generation

In Section III-A, we have confirmed that the second half subcarrier parts of Antennas A and B are also single carrier signals as long as the first half subcarrier parts are single carrier signals. The remaining consideration is how to set the phase shift terms $\zeta^{(A)}$ and $\zeta^{(B)}$ in Fig. 3 so that the first half subcarrier parts (the first and third double summation terms in (8) and (9)) have the single carrier effect. To do this, we need to find the relation between ($\zeta^{(A)}$, $\zeta^{(B)}$) and the ITSM-conditioned (η, μ) given in (6) and (7). By matching the first double summation term in (13) with the upper (on time) signal branch in Fig. 2, and by matching the third double summation term with the lower (half symbol-delayed) signal branches, we can make $s(t)$ in Fig. 2 equal to the first half subcarrier part of $s^{(A)}(t)$ in (13) by setting the terms in Fig. 2 as follows:

$$N_D = N/2, \quad S_1 = 0, \quad S_2 = 0, \tag{23}$$

$$\eta_{n,m} = \zeta^{(A)}_{n,2m}, \tag{24}$$

$$\mu_{n,m} = (-1)^n\zeta^{(A)}_{n,2m+1}. \tag{25}$$

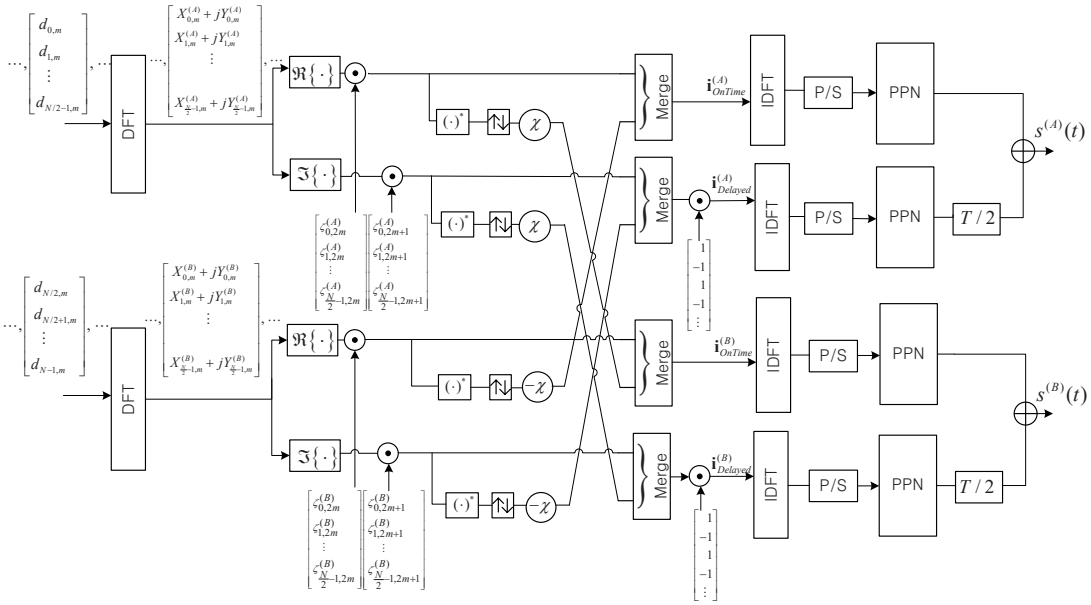

Fig. 3. Transmitter of the ITSM-conditioned and DFT-spread Alamouti-coded FBMC.

If we take the ITSM conditioned pair (η, μ) given in (6), then from (24) and (25), we need to set

$$\zeta^{(A)}_{n,2m}(=\eta_{n,m}) = j^n, \tag{26}$$

$$\zeta^{(A)}_{n,2m+1}(=(-1)^{-n}\mu_{n,m}) = j^{n+1} \tag{27}$$

and for the other ITSM conditioned pair (η, μ) in (7), we need to set

$$\zeta^{(A)}_{n,2m} = (-j)^n, \tag{28}$$

$$\zeta^{(A)}_{n,2m+1} = j(-j)^n. \tag{29}$$

Through the same analysis, two kinds of ITSM conditioned pairs for the half subcarrier part of Antenna B, i.e., $(\zeta^{(B)}_{n,2m}, \zeta^{(B)}_{n,2m+1})$ are also given as the right hand sides of ((26),(27)) and ((28),(29)).

By switching the pair $(\zeta_{n,2m}, \zeta_{n,2m+1})$ between ((26),(27)) and ((28),(29)) at each antenna, we can generate four kinds of ITSM-conditioned signal pairs for the two Antennas, i.e., $(s^{(A)}(t),\ s^{(B)}(t))$. From the viewpoints of the four element-by-element multiplier output stages in Fig. 3, switching $(\zeta_{n,2m}, \zeta_{n,2m+1})$ between ((26),(27)) and ((28),(29)) is equivalent to fixing $(\zeta_{n,2m}, \zeta_{n,2m+1})$ to ((26),(27)) and then switching between the case of multiplying $[1, -1, 1, -1, \cdots]$ to DFT spread symbols and the case of just bypassing DFT spread symbols as shown in Fig. 4. The switching control bits S_A and S_B in Fig. 4 determine whether or not to multiply $[1, -1, 1, -1]$ to DFT spread symbols of the first half subcarrier parts of Antennas A and B, respectively.

In addition to the four kinds of the ITSM-conditioned signal pairs $(s^{(A)}(t),\ s^{(B)}(t)\ )$ mapped to each of the four combinations of the control bit pair (S_A, S_B), we have another version for each of the four ITSM conditioned signal pairs by switching the $T/2$ delay from the second (from the top in Fig. 3) and the fourth PPN outputs to the first and the third PPN outputs as shown in Fig. 4. Note that as the Alamouti-coded symbols in the two antennas should be time synchronized, the delay switching control bit S_2 should be the same for the two antennas. Consequently, in total, eight kinds of ITSM-conditioned signal pairs of the two Antennas are generated by setting the three switching control bits (S_A, S_B, S_2) to one of the eight possible three bit word set, i.e., $\{(0, 0, 0), (0, 0, 1), \cdots (1, 1, 1)\}$, and we have to jointly minimize the PAPR of both antennas over the eight candidate pairs. We employ the min-Max method, i.e., we select the candidate version, which minimizes the global maximum power of the two TX antennas as follows:

$$(S_{A,min}, S_{B,min}, S_{2,min}) = \underset{\substack{(S_A, S_B, S_2) \\ \in \{(0,0,0), \cdots, (1,1,1)\}}}{\arg\min} \left[\max\left(p^{(A)}_{(S_A,S_B,S_2)}, p^{(B)}_{(S_A,S_B,S_2)}\right)\right] \tag{30}$$

where $p^{(A)}_{(S_A,S_B,S_2)}$ and $p^{(B)}_{(S_A,S_B,S_2)}$ denote the peak powers of Antennas A and B over the time zone the considered frame signal spans, respectively for the case when the three switching control bits are given as (S_A, S_B, S_2).

As observed in [11], the subframe-wise candidate selection enhances the PAPR reduction gain. In the case of subframe partitioning, the two considerations should be added to the algorithm. Firstly, we have to find the subframe signal candidate having the minimum peak power *after* adding (concatenating) each of the subframe signal candidates to the preceding subframes. This is because, the consecutive subframes are overlapped in the time domain due to the pulse shaping. Secondly, to maintain the FBMC signal format, j $(=\sqrt{-1})$ should be additionally multiplied to the subframe signal candidate if the switching control bit S_2 for the candidate is 1 [11]. This is why conditional j multiplications are included in the final stage prior to subframe concatenation in Fig. 4.

In the receiver side, according to the three received switching control bits $(S_{A,min},\ S_{B,min},\ S_{2,min}\ )$, all the processing

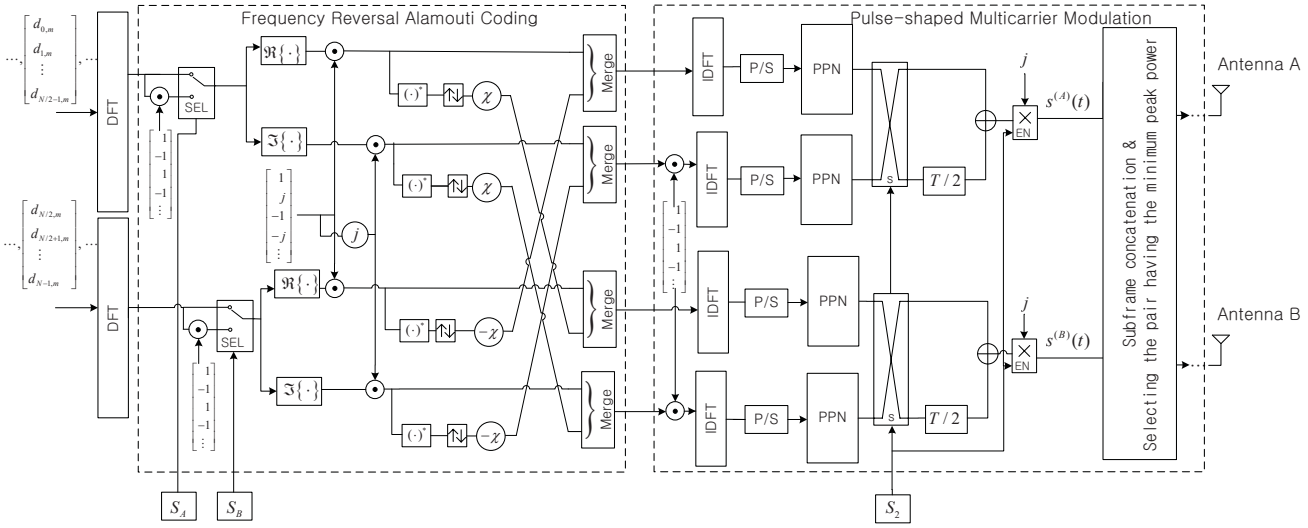

Fig. 4. Transmitter of the proposed Alamouti-coded LP-FBMC.

done in the transmitter side is recovered in the reverse order. Thus, the implementation is straightforward. Fig. 5 shows the implementable low level receiver structure of the proposed Alamouti-coded LP-FBMC. Assuming $S_{2,min} = 0$, the dashed box performs FRAC decoding for the demodulated version of on-time FBMC symbol. The demodulated version of $T/2$-delayed FBMC symbol undergoes identical processing, which is specified in the single box below the dashed box. The only two things should be modified at the inputs to this lower single box compared to the dashed box. Firstly, as the phase shift terms multiplied to the on-time and $T/2$-delayed FBMC symbols in the transmitter are different, as shown in Fig. 4, they should be set different in order to be compensated in the receiver as well. Secondly, as the sign of every other element of the IDFT inputs for $T/2$-delayed FBMC symbols in the transmitter is inverted, the sign of every other element of the DFT output fed into the lower single box of the receiver should be inverted for compensating this. Responding to expanding-and-add operation of the PPN in the transmitter for pulse shaping, the PPN in the receiver employs folding-and-accumulation operation for matched filtering [28].

D. Complexity-reduced equivalent structure

If we implement the transmitter given in Fig. 4 as it is, we need to perform four times each of the four IDFT-PPN branches. This is because, there are four possible cases of the switching control bit pair (S_A, S_B), and for each of the cases, the corresponding IDFT inputs are differently generated. Consider an alternative implementation where we skip one (say the upper one in Fig. 4) of the two conditional multiplications of $[1, -1, 1, -1, \cdots]$ at the DFT output stages but introduce the conditional multiplications of $[1, -1, 1, -1, \cdots]$ to the four IDFT input stages. With this alternative implementation, we can still make four kinds of ITSM candidate signal pairs for the first half subcarrier parts of two antennas. In addition, we can employ the property that the multiplication of $[1, -1, 1, -1, \cdots]$ to the IDFT input is equivalent to swapping the first and second halves of the IDFT output [11], as shown in Fig. 6. The four blocks named *Half Swap or Bypass* in Fig. 6 selectively perform swapping of IDFT outputs according to the switching control bit S_1. Note that in Fig. 4, there is already another multiplication of $[1, -1, 1, -1, \cdots]$ to the second (to the top) and fourth IDFT inputs for ITSM condition. These multiplications are equivalently replaced by half vector swapping at the second and fourth IDFT output stages. Then, applying *Half Swap or Bypass* switch to these already half-swapped outputs is equivalent to simply negating the switching control input S_1 to those (the second and fourth) *Half Swap or Bypass* blocks as shown in Fig. 6. Consequently, in the structure shown in Fig. 6, the four IDFT blocks are performed only twice, not four times, and therefore we can reduce the IDFT calculation burden to one half of that required in the structure shown in Fig. 4. The term χ in Fig. 4 is set to j in Fig. 6. The modification to the version with χ=-j is straightforward.

Yet, there are two important considerations to accomplish perfect equivalence between the structures shown in Fig. 4 and Fig. 6. Firstly, in Fig. 6, the DFT spread data vector in Antenna B undergoes conditioned multiplication by $[1, -1, 1, -1, \cdots]$ twice (by S_0 and S_1), whereas in Fig. 4, it undergoes conditioned multiplication just once by S_B. Therefore, we have the following equivalence between the switching control bits in Fig. 4 and Fig. 6 : $S_B = (S_0 + S_1)$-modulo-2 while $S_A = S_1$. Secondly, multiplying $[1, -1, 1, -1, \cdots]$ to the DFT spread data vector in one antenna branch in Fig. 4 is equivalent to multiplying $[-1, 1, -1, 1, \cdots]$ (not $[1, -1, 1, -1, \cdots]$) to the second half parts of the IDFT inputs of the other TX antenna branch due to the frequency reversal operation. Considering these two factors, the TX signals by the switching control bit pair (S_0, S_1) in Fig. 6 are equivalently generated by setting the switching control bit pairs (S_A, S_B) and the term χ in Fig. 4 as shown in Table. I.

Note that in Fig. 4, χ is multiplied to the frequency reversal part. Furthermore, from Table I, it should be noted that χ in Fig. 4 changes according to S_1 in Fig. 6. This implies that

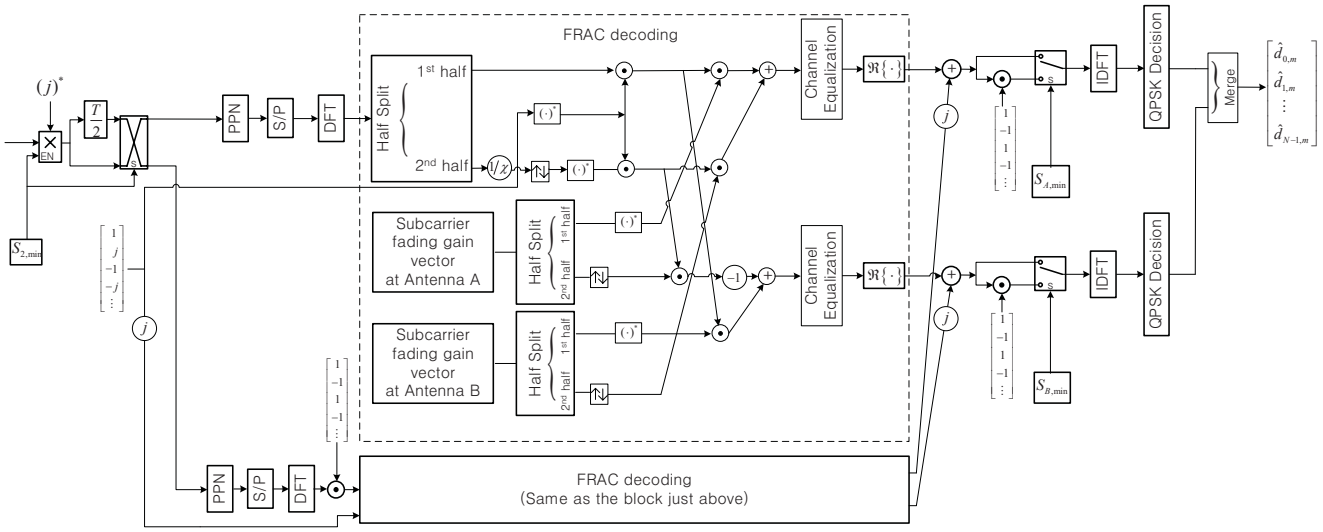

Fig. 5. Receiver of the proposed Alamouti-coded LP-FBMC.

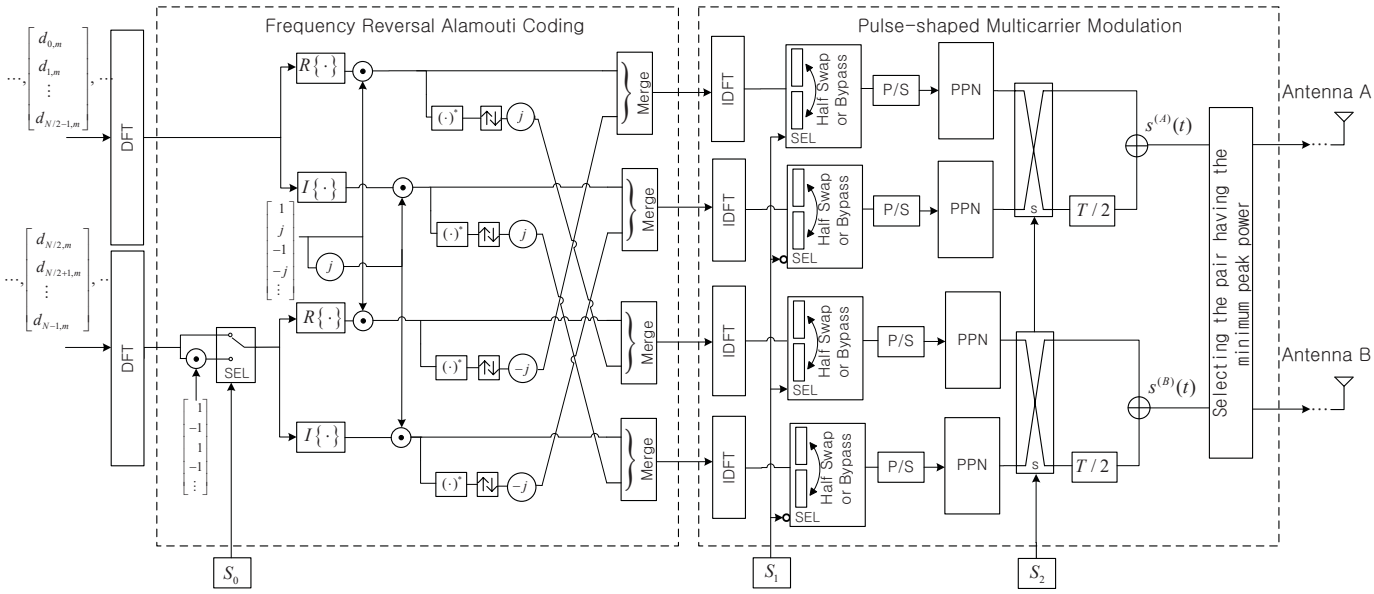

Fig. 6. Complexity-reduced version of Fig. 4 for the frame-wise candidate selection.

TABLE I
EQUIVALENT MAPPING OF THE SWITCHING CONTROL BITS IN FIG. 4 AND FIG. 6

(S_0, S_1) in Fig. 6	(S_A, S_B) and χ in Fig. 4
(0, 0)	(0, 0), $\chi = j$
(0, 1)	(1, 1), $\chi = -j$
(1, 0)	(0, 1), $\chi = j$
(1, 1)	(1, 0), $\chi = -j$

the Alamouti code structures for S_1 =0 and 1 in Fig. 6 are different. Thus, if consecutive subframes are generated with different settings of S_1 in Fig. 6 and the subframe boundaries are overlapped by the pulse tails, the self ICI cancellation by the frequency reversal Alamouti coding does not work in the subframe boundary. Therefore, in the case of subframe-wise candidate selection, we have to use the structure shown in Fig. 4 and not the one shown in Fig. 6.

E. Subblock partitioning for frequency selective fading

The self ICI cancellation property of the frequency reversal Alamouti-coded symbol arrangement shown in Fig 1 is valid only under the condition that each frequency reversal pair has an identical fading coefficient, i.e., flat fading within the frequency reversal half band pairs. In frequency selective fading environments, we can approximately achieve flat fading within the frequency reversal half band pairs by properly dividing the entire allocated band into multiple subbands. Then, by separately applying the frequency reversal Alamouti coding to each subband, we can restore the self ICI cancellation property. As the peak power reduction by DFT spreading is less effective

for smaller DFT sizes, we employ partitioning not to the input data symbols but to the DFT spread data symbols in order to maintain the DFT size. Fig. 7 shows the final version of the Alamouti-coded LP-FBMC transmitter including subblock partitioning. The variable L denotes the number of partitions. Each of the L partitioned DFT output with a length of $P = \frac{N/2}{L}$ separately goes through *'Frequency reversal Alamouti coding'* shown in the left dashed box in Fig. 6 (Fig. 4 for subframe-wise candidate selection case) and then, each of the four outputs with length $2P(= N/L)$ are separately merged in groups over the entire subblocks. To avoid inter-antenna inter-subblock interference at the subblock edge, null subcarriers are inserted in between consecutive subblocks. Finally, the four merged outputs go through the *'Pulse-shaped multicarrier modulation'* whose details are shown in the right side dashed box in Fig. 6 (Fig. 4 for subframe-wise candidate selection case).

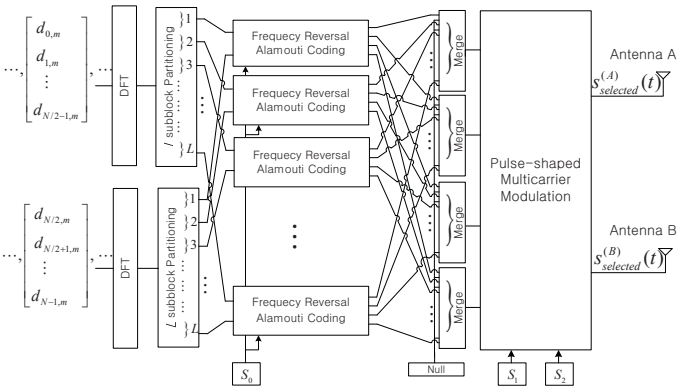

Fig. 7. Final version of the Alamouti-coded LP-FBMC transmitter including subblock partitioning.

For PHYDYAS pulse with an overlapping factor $K = 4$ which is employed in this paper, the intercarrier interference is nonzero only to the very next (left and right) subcarriers (see Table 2 in [14] or Table 1 in [19]). This explains why in the multiuser (or multi-node) FBMC systems using PHYDYAS pulse, only one null subcarrier is inserted in between the adjacent users' band [29–32]. Likewise, in the proposed Alamouti-coded LP-FBMC with subblock partitioning, just one null subcarrier is sufficient between the consecutive subblocks for zero inter-subblock interference between the two TX antennas. Thus, there are $L-1$ null subcarriers out of a total of $N+L-1$ subcarriers, and the data rate loss due to null subcarriers is equal to $(L-1)/(N+L-1)$.

IV. Derivation of the Single Carrier Form Expression

Assuming the ITSM condition given in (26) and (27) and doing some math, $s^{(A)}(t)$ in (10) is generalized into the subblock-partitioned case as follows:

$$s^{(A)}(t) = \left\{ \sum_{l=0}^{L-1} \sum_{n=0}^{P-1} \left\{ X^{(A)}_{lP+n,m} + jY^{(A)}_{lP+n,m} \right\} e^{j\frac{2\pi(l(2P+1)+n)}{T}\left(t+\frac{T}{4}\right)} \right.$$
$$\left. -\chi \sum_{l=0}^{L-1} \sum_{n=0}^{P-1} \left\{ X^{(B)}_{lP+n,m} - jY^{(B)}_{lP+n,m} \right\} e^{j\frac{2\pi(l(2P+1)+(2P-1)-n)}{T}\left(t+\frac{T}{4}\right)} \right\} \quad (31)$$

where $LP = N/2$. Recall that $X^{(A)}_{(0:N/2-1),m} + jY^{(A)}_{(0:N/2-1),m}$ and $X^{(B)}_{(0:N/2-1),m} + jY^{(B)}_{(0:N/2-1),m}$ are the DFT outputs of the first and second halves of the data symbol vector $d_{(0:N-1),m}$, respectively and thus they are written as follows:

$$X^{(A)}_{n,m} + jY^{(A)}_{n,m} = \sum_{k=0}^{N/2-1} d_{k,m} e^{-j2\pi nk/(N/2)} \quad (32)$$

$$X^{(B)}_{n,m} + jY^{(B)}_{n,m} = \sum_{k=0}^{N/2-1} d_{N/2+k,m} e^{-j2\pi nk/(N/2)}. \quad (33)$$

Substituting (32) into (31), we can show that the first double summation term in (31) is written as:

$$\sum_{l=0}^{L-1} \sum_{n=0}^{P-1} \left\{ X^{(A)}_{lP+n,m} + jY^{(A)}_{lP+n,m} \right\} e^{j\frac{2\pi(l(2P+1)+n)}{T}\left(t+\frac{T}{4}\right)}$$
$$= \sum_{k=0}^{N/2-1} d_{k,m} \sum_{l=0}^{L-1} \sum_{n=0}^{P-1} e^{j\frac{2\pi(l(2P+1)+n)}{T}\left(t+\frac{T}{4}\right)} e^{-j\frac{2\pi}{N/2}(lP+n)k}$$
$$= \sum_{k=0}^{N/2-1} d_{k,m} z_k\left(t+\frac{T}{4}\right) \quad (34)$$

where we denote the last double summation term by a pulse $z_k\left(t+\frac{T}{4}\right)$. Rearranging the double summation and then, using the summation formula for the geometric sequence, we can show the following:

$$z_k(t) \left(\triangleq \sum_{l=0}^{L-1} \sum_{n=0}^{P-1} e^{j\frac{2\pi(l(2P+1)+n)}{T}t} e^{-j\frac{2\pi}{N/2}(lP+n)k} \right)$$
$$= f_L\left(\alpha(t-\beta k)\right) f_P\left(\gamma(t-\delta k)\right) \quad (35)$$

where $\alpha = \pi\frac{2P+1}{T}$, $\beta = \frac{2P}{2P+1}\frac{T}{N}$, $\gamma = \frac{\pi}{T}$, $\delta = \frac{2T}{N}$ and

$$f_\lambda(t) = \frac{\sin(\lambda t)}{\sin(t)} e^{j(\lambda-1)t} \quad (36)$$

whose magnitude follows the Dirichlet sinc pulse [33]. Consequently, the magnitude of $z_k(t)$ is the product of two Dirichlet sinc pulses whose centers (peak positions) increase with steps of $\beta(\approx T/N)$ and $\delta(= 2T/N)$, respectively as k increases.

In Fig. 8, the pulse magnitude $|z_k(t)|$ is plotted for various numbers of subblocks L with $N = 256$. For reference, the PHYDYAS prototype pulse $p(t)$ is plotted for one symbol duration at the top of Fig. 8. It is shown that $z(k)$ is much narrower than $p(t)$ and the peak positions of $z(k)$ shift according to k while the narrow pulse shapes are maintained. Note that as L increases, the peaks are split into multiple positions, and the pulses become even narrower. This is explained as follows. The entire signal bandwidth is proportional to $N+L-1$, i.e., the total number of subcarriers including the inter-subblock nulls. Hence, the pulse width which is inversely proportional to the bandwidth decreases as L increases. Meanwhile, the denominator of the first factor in (35), i.e., the denominator $f_L\left(\alpha(t-\beta k)\right)$ is given as $\sin\left(\alpha(t-\beta k)\right)$ whose period is equal to $2\pi/\alpha = 2T/(2P+1) = 2LT/(N+L)$. Thus, the pulse peaks appear at every $LT/(N+L)$ seconds as we are taking the absolute value of the pulse. This results in multiple peaks during one symbol duration and the peaks decrease as their locations are getting away from the main peak due to the

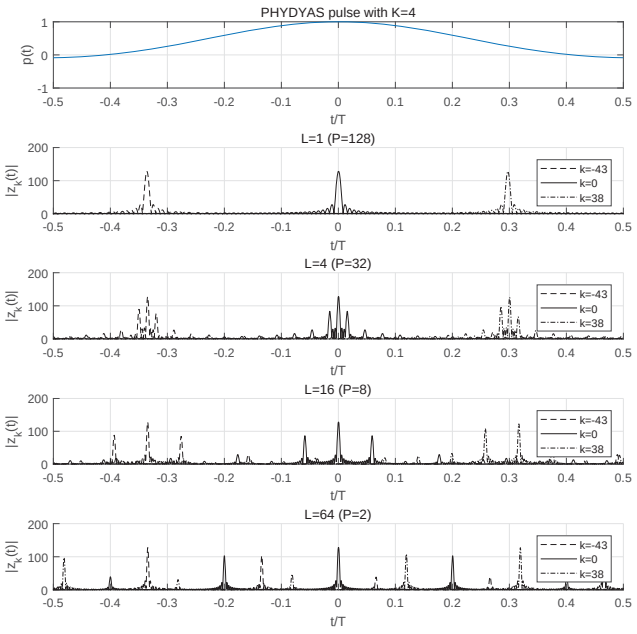

Fig. 8. Pulse magnitude $|z_k(t)|$ for various number of subblocks L and three different ks with $N = 256$

denominator in the second factor in (35), i.e., the denominator of $f_P(\gamma(t-\delta k))$ which is given as $\sin((\pi/T)(t-\delta k))$. For the case with $L = 1$, the peaks are placed back-to-back but the peaks gradually decrease. Hence, the pulse looks as if there is only one peak.

Overall, the first double summation term in (31) is actually a single carrier signal, which sequentially transmits the data symbol-multiplied narrow pulses. With a simple modification, it is straightforward that the second double summation term in (31) is another single carrier signal. This can be also conjectured from our preliminary analysis made in Section III-A that with a condition that the first half subcarrier part (= the first double summation term in (31)) is a single carrier signal, the second half subcarrier part (= the second double summation term) is a single carrier signal as well. Similarly, we can show that the other antenna signal, i.e., $s^{(B)}(t)$ is equivalent to the single carrier signal. This is because, in order to get the expression of $s^{(B)}(t)$ from (31), we only need to exchange the antenna indices and toggle the sign of the second double summation term. In addition, this single carrier effect holds for the other ITSM condition in (28) and (29), as we only need to change $T/4$ in (31) into $-T/4$ for this ITSM condition. Summing up, even with subblock partitioning, the proposed Alamouti-coded LP-FBMC still achieves the single carrier effect of DFT spreading, and therefore we expect substantial PAPR reduction, which we confirm in the simulation result section.

V. Complexity Analysis

Complexity comparison between FBMC and cyclic prefix (CP)-OFDM has been intensively assessed in the literature such as [29, 34]. As for the comparison between the DFT-spread versions or Alamouti-coded versions of FBMC and CP-OFDM, it is straightforward that the complexity gap just slightly decreases because the DFT spreading/despreading or Alamouti coding/decoding add the common amount of complexities to FBMC and CP-OFDM. The overall comparison of the various performance measures including complexity between Alamouti-coded versions of CP-OFDM, DFT-S-OFDM, FBMC and the proposed scheme are made in Section VII.

This section focuses on calculating complexity of the proposed Alamouti-coded LP-FBMC and compare it to that of FRAC-FBMC which is the target system in this paper. First as for the transmitter complexity, each of the two TXs of FRAC-FBMC needs the identical number of real multiplications (RMs) to that of FBMC because the Alamouti coding process does not require multiplication. Thus, FRAC-FBMC transmitter requires $2 \times \left(8N\log_2(2N) - 12N + 8\right)$ and $2 \times 8NK$ RMs per FBMC symbol for 2 IDFTs and 2 PPNs, respectively. The transmitter of the proposed scheme with single candidate in Fig. 4 additionally needs only one DFT at the input stage which needs $2N\log_2(N/2) - 3N + 8$ RMs. With eight candidates, the transmitter of the proposed scheme in Fig. 4 needs 4 times of IDFTs and PPNs for FRAC-FBMC due to four possible cases of the switching control bit pair (S_A, S_B). On the other hand, the complexity reduced transmitter of the proposed scheme in Fig. 6 save IDFT operations to one-half of that of the transmitter in Fig. 4 by moving the one of the switches (S_A, S_B) next to the IDFT stages. Overall, the numbers of RMs for the transmitters of FRAC-FBMC, the proposed scheme in Fig. 3 with single candidate, the proposed scheme in Fig. 4 with eight candidates and the complexity reduced version in Fig. 6 with eight candidates are $80N+32N\log_2(2N)+32$, $74N+32N\log_2(2N)+4N\log_2(N/2)+48$, $314N+128N\log_2(2N)+4N\log_2(N/2)+144$ and $410N+64N\log_2(2N)+4N\log_2(N/2)+80$, respectively and are plotted in Fig. 9(a). It is shown that the transmitter of the proposed scheme with single candidate has almost the same complexity as that of FRAC-FBMC because the complexity overhead for DFT spreading is negligible. On the other hand, with eight candidates, the transmitter of the proposed scheme in Fig. 4 needs roughly four times complexity compared to FRAC-FBMC. However, the transmitter in Fig. 6 with eight candidates substantially save complexities (about 34%) although it is still higher than that of FRAC-FBMC. The high transmitter complexity of the proposed scheme with eight candidate is not surprising. This is because all the multiple candidate-based PAPR reduction schemes such as PTS and SLM as well as the proposed scheme repeat some parts of modulation processes multiple times to choose the candidate with minimum peak power and thus, they all inevitably undergo significant complexity increase.

Secondly as for the receiver complexity, FRAC-FBMC needs $2 \times 8NK$, $2 \times (16N\log_2(4N) - 24N + 8)$ and $8N$ RMs per FBMC symbol for 2 PPNs, 2 IDFTs and Alamouti decoding, respectively. Given side information, the proposed scheme also goes through 2 PPNs, 2 IDFTs and Alamouti decoding at each FBMC symbol and additionally requires

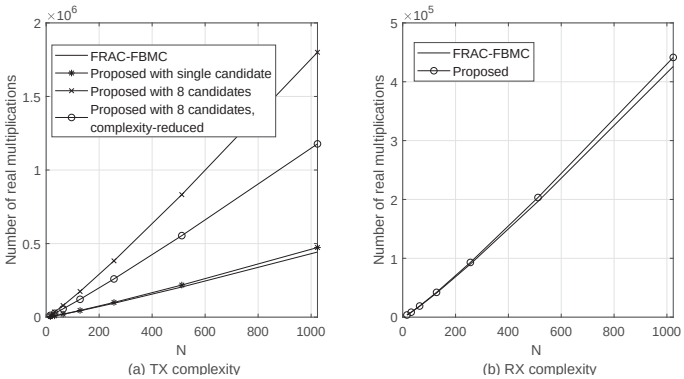

Fig. 9. Complexity of FRAC-FBMC [25] and the proposed scheme, OQPSK.

one IDFT at the final stage for despreading DFT-spread symbols as shown in Fig. 5. Overall, the numbers of RMs for the receivers of FRAC-FBMC and the proposed scheme are $32N + (32N\log_2(4N)) + 16$ and $29N + (2N\log_2(N/2)) + (32N\log_2(4N)) + 24$ respectively and are plotted in Fig. 9(b). Note that the receiver complexity gap between the FRAC-FBMC and the proposed scheme is negligible because the complexity overhead for DFT despreading (=IDFT) is negligible.

VI. Simulation results

In this study, we are interested in applying Alamouti code to FBMC while maintaining the intrinsic advantages of FBMC over the OFDM-based scheme such as excellent OOB suppression capability. Therefore, in this section, we focus on FBMC-based schemes for performance comparison in terms of PAPR and BER. For references, OFDM-based Alamouti-coded schemes, i.e., Alamouti-coded versions of CP-OFDM and DFT-S-OFDM are also included in performance comparison. However, for a balanced comparison with OFDM-based schemes, we need to consider not only BER and PAPR but also the other important aspects and the complexity. This will be addressed in Section VII.

Due to the intrinsic inter-antenna inter-carrier interference of FBMC, only a few Alamouti-coded FBMC schemes have been reported so far such as the recent researches [15–17, 22, 23]. As we mentioned in the Introduction section, the most recent scheme in [25] resolves the issues in the schemes proposed in [15–17, 22, 23] and outperforms them in terms of computational complexity, latency and data rate. Therefore, as a main reference for assessing the performance of our proposed scheme, we take the one in [25], which we refer to as FRAC-FBMC and was introduced in Section II-A.

A. PAPR performance

Fig. 10 shows the CCDF (complementary cumulative distribution function) curves of the PAPR of FRAC-FBMC and the proposed scheme for the case when N=256, the PHYDYAS pulse with an overlapping factor K=4 is employed for the spectrum localization pulse $p(t)$, and the data symbol $d_{n,k} = \pm 1 \pm j$. For each curve, the transmit waveforms of 10^5 frames are generated. As for the proposed scheme, the following three versions are simulated.

- Case when only ITSM-conditioned DFT spreading and FRAC are considered as shown in Fig. 3, and no candidate selection is included.
- Case when frame-wise eight candidate generation/selection is added, as shown in Fig. 4.
- Case when subframe-wise eight candidate generation/selection is added. Specifically, for maximum PAPR reduction gain by subframing, we set the subframe size equal to 1, i.e., we employed actual symbol-wise eight candidate generation and selection.

For fair comparison, the subblock partitioning in Fig. 7 (to cope with the selective fading) is employed to FRAC-FBMC as well as the proposed scheme. In all the three versions of the proposed scheme, as the number of partitions L increases, the PAPR increases to some extent. This is because as shown in Fig. 8, the number of pulse peaks in the single carrier-formed pulse given in (35) increases as L increases, and the summation of the pulse shaped symbols with different positions results in more fluctuation in the signal amplitude. However, even with maximum subblock partitioning (L = 64), the increase in gap of PAPR remains less than 0.5 dB, and this is the case with all the three versions of the proposed scheme. In addition, for the versions with eight candidate selection, the PAPR rapidly converges as L increases from 1. On the other hand, in FRAC-FBMC, subblock partitioning has negligible impact on PAPR performance as there is no DFT spreading.

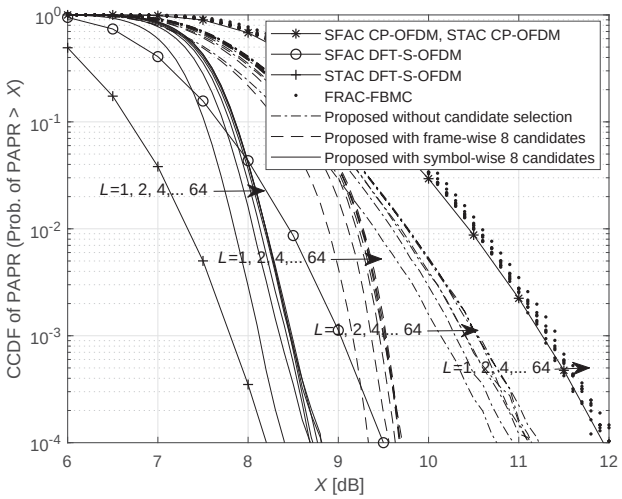

Fig. 10. CCDFs of PAPR for FRAC-FBMC [25] and the proposed scheme, N=256, M=32, OQPSK.

Note that even without candidate selection, the proposed scheme achieves about 1 dB PAPR reduction at a CCDF of 10^{-3} compared to FRAC-FBMC. If we include the eight candidate selection idea to the proposed scheme, the frame-wise scheme achieves about 2 dB PAPR reduction compared to FRAC-FBMC. If we employ the symbol-wise eight candidate selection idea in order to enhance PAPR reduction further, the PAPR reduction gain of the proposed scheme over FRAC-FBMC increases to about 3 dB. To inform the receiver about the selected candidate, a 3 bit side information should be sent for every FBMC symbol in the symbol-wise selection

scheme, whereas it should be sent only for every frame in the frame-wise selection scheme. However, 3 bit side information per FBMC symbol is still quite small compared to the nominal amount of side information in the conventional candidate selection-based PAPR reduction scheme, and it is still attractive in practical systems.

For the references, Alamouti-coded versions of CP-OFDM and DFT-S-OFDM are also simulated and are included in Fig. 10. As both space frequency Alamouti-coded (SFAC) CP-OFDM and space time Alamouti-coded (STAC) CP-OFDM have no DFT-spreading as in FRAC-FBMC, they have the almost the same PAPR as that of FRAC-FBMC. On the other hand, SFAC DFT-S-OFDM and STAC DFT-S-OFDM achieve significant PAPR reduction because they inherit the single carrier effect of DFT-S-OFDM. Also, it is shown that while STAC DFT-S-OFDM has lower PAPR than that of the proposed scheme, SFAC DFT-S-OFDM has higher PAPR than that of the proposed scheme with symbol-wise eight candidate selection. This is explained as follows. Firstly, the SFAC DFT-S-OFDM and the proposed scheme have higher PAPR than that of STAC DFT-S-OFDM due to a common factor that two DFT spread data vectors are interlaced by Alamouti coding in the subcarrier axis. However, secondly, the proposed scheme has an additional PARR reduction gain by candidate selection compared to SFAC DFT-S-OFDM.

Based on the fact that the transmit signal of the proposed scheme appears as a summation of two single carrier (SC) signals, we can get an insight on the PAPR of the proposed scheme. Consider a case when the two data modulated SC signals are summed. Then, while the average power increases twice compared to one SC signal, the instantaneous peak power increases four times at maximum because the pulse peak points of the two signals are possibly added and result in twice amplitude. Consequently, PAPR increases up to 3 dB in worst case. However, the PAPR performance is measured not by worst case PAPR but by the CCDF of PAPR which is determined by the distribution of the instantaneous signal power. Therefore, the PAPR gap in CCDF curves of the proposed scheme and the LP-FBMC whose transmit signal is one SC signal is much less than 3 dB. This is confirmed by comparing CCDF curves in Fig. 7 of [11] and the ones in Fig. 10.

B. Bit error rate performance

Fig. 11 shows the BER curves of FRAC-FBMC (in the left hand side) and the proposed scheme (in the right hand side) under Rayleigh flat fading channel, ITU-R Pedestrian-A, and ITU-R Vehicular-A multipath channels [35]. Two transmit antennas and one receive antenna configuration is considered. The subcarrier spacing is set to 15 kHz in accordance with the LTE/LTE-A standard. The Alamouti decoding is followed by a per-carrier one tap equalization with minimum mean squared error (MMSE) criterion. As a reference, the theoretical BER curve of Alamouti code is included in each subplot. For a neat presentation, we insert a legend only to the first subplot. At each simulated BER, 2×10^4 bit errors are gathered.

Various numbers of the half subblock size $P\,(=\frac{N}{2L})$ from $N/2$ to 2 are simulated. We note a common trend in all

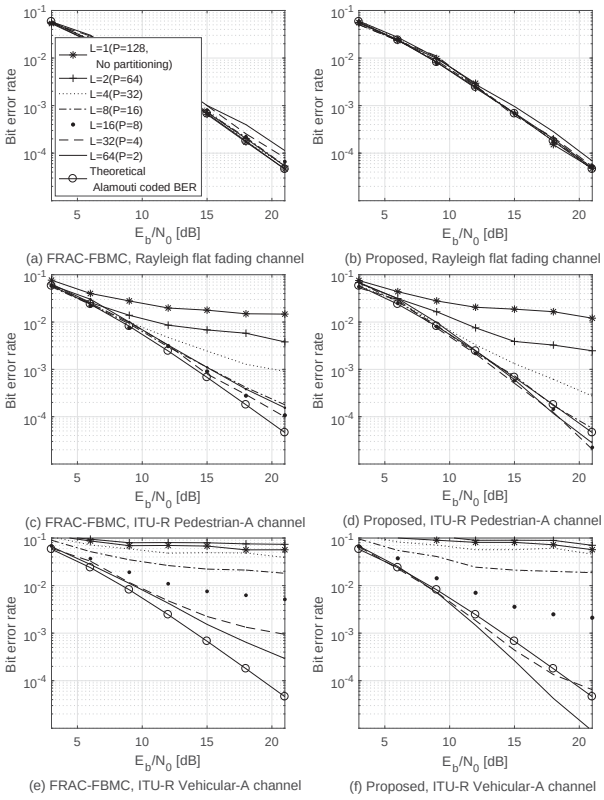

Fig. 11. BER curves for FRAC-FBMC [25] and the proposed scheme for various subblock size, N=256, M=32, OQPSK.

the subfigures in Fig. 11 that the optimum P achieving the minimum BER does not change over the SNR range. As the second common trend to both FRAC-FBMC and the proposed scheme, it is shown that as the channel selectivity increases, the BER becomes more sensitive to P. With a proper setting of P, the BER approaches the theoretical Alamouti-coded BER. It is remarkable that in the multipath channels, the proposed scheme with a proper P achieves even better BER than the theoretical Alamouti-coded BER. This is because, the theoretical Alamouti code achieves a diversity order of only two, whereas the DFT spreading and despreading processes of the proposed scheme achieves additional diversity in the frequency domain, and this frequency diversity becomes greater in more selective fading channels.

In order to find the optimal P and compare the BER performance on the basis of the best setting of P, the vertical cuts of BER curves at two different SNR points are horizontally plotted as functions of P in Fig. 12. In the flat fading channel, as the half subblock size P decreases from 128 (=$N/2$, no subblock partitioning), the BER increases. This is because, partitioning into more subblocks results in more inter-half subblock interference. On the other hand, in frequency selective fading, the BER for the no subblock partitioning case (P=128) is significantly large, due to the violation of the quasi static fading assumption within the band to which the

frequency reversal Alamouti-coded symbol pair belongs. This problem is more serious in more selective fading channels. However, note that by partitioning and decreasing the half subblock size P from 128, we can significantly decrease the BER. On the other hand, if the half subblock size is excessively smaller than the coherence bandwidth (like P=2 in Pedestrian-A channel), then the BER increases again due to the same reason we mentioned for the flat fading channel case above, i.e., more inter-half subblock interference. In the Pedestrian-A channel, the proposed scheme with P = 2, 4 and 8 achieves even lower BER than the theoretical Alamouti-coded BER. In the Vehicular-A channel, the proposed scheme with P = 2 or 4 achieves even lower BER than the theoretical Alamouti-coded BER. Note that with P = 4, FRAC-FBMC also achieves the minimum BER for Pedestrian-A channel; however, the BERs are still larger than the theoretical Alamouti-coded BER.

For the references, Alamouti-coded versions of CP-OFDM and DFT-S-OFDM are also simulated and are included in Fig. 12. As Alamouti-coded CP-OFDM has no DFT-spreading and thus no frequency diversity, its BER is identical to the theoretical Alamouti-coded BER. On the other hand, Alamouti-coded DFT-S-OFDM achieves significant BER improvement in the multipath fading channel because it exploits the frequency diversity in addition to basic diversity of Alamouti code as in the proposed scheme. Besides, Alamouti-coded symbol pair in DFT-S-OFDM undergoes almost identical fading gains and thus, there is no self interference in Alamouti-decoding. Therefore, the BER is even lower than that of the proposed scheme. However, for the less selective fading channels like Pedestrian-A channel, the BER gap between Alamouti-coded DFT-S-OFDM and the proposed scheme with optimal P is relatively small. In addition, for a balanced comparison with OFDM-based schemes, we need to consider not only BER and PAPR but also the other important aspects along with the complexity. This will be addressed in Section VII.

C. Data rate loss performance

As one null subcarrier is inserted in between the subblocks and the subblock size is equal to $2P$, the data rate loss by subblock partitioning is $1/2P$. For P = 4 or 8, the data rate loss is 12.5 % or 6.25 %, respectively. This data rate loss is lower than the typical data rate loss of OFDM due to insertion of guard interval and guard subcarriers. We can further decrease the data rate loss by decreasing the frequency spacing Δf or by increasing the subblock bandwidth B_s to increase P. Meanwhile, under the constraint to achieve quasi-flat fading, the optimal B_s for minimum BER needs to be proportional to the channel coherence bandwidth B_c. If we take the BER performance of the proposed scheme with P= 8 and Δf= 15kHz at the Pedestrian-A channel in Fig. 12 as a target performance and aim to achieve this performance for the general frequency selective channel, the equivalent B_s denoted by $B_{s,eq}$ is given by a simple proportional rule as:

$$\begin{aligned} B_{s,eq} &= \frac{B_c}{B_{c,Ped-A}} \times (B_s \text{ for } P = 8 \text{ and } \Delta f = 15\text{kHz}) \\ &= \frac{B_c}{B_{c,Ped-A}} 240 \text{ kHz} \end{aligned} \quad (37)$$

where $B_{c,Ped-A}$ denotes the coherence bandwidth of the Pedestrian-A channel. For a given $B_{s,eq}$ and Δf, P is equal to $(B_{s,eq}/\Delta f)/2$, and thus from (37), we have

$$P = \frac{120 B_c}{(\Delta f \text{ in [kHz]})\, B_{c,Ped-A}} \quad (38)$$

and the data rate loss is given as:

$$\text{data rate loss} = 1/2P = \frac{\Delta f \text{ in [kHz]}}{240} \times \frac{B_{c,Ped-A}}{B_c}. \quad (39)$$

As expected, the data rate loss of the proposed scheme inversely decreases as B_c increases. Thus, for less selective channels, i.e., larger B_c, the data rate loss of the proposed scheme is smaller. In the case of severer multipath channel, i.e., smaller B_c, we can maintain the acceptable data rate loss by properly decreasing Δf. Meanwhile, for Δf, there might be the other issues depending on application or channel environment. For instance, in the fast fading channels or with high Doppler rate such as in mmWave band, Δf should be sufficiently large to keep FBMC symbol duration shorter than the channel coherence time and this increases data rate loss. Note that because B_c as well as Δf is much larger in mmWave band, the overall data rate loss in mmWave band can be compromised.

VII. Overall comparison among the various Alamouti-coded multicarrier systems

For balanced (un-biased) comparison among the different systems, we need to consider various performance aspects and complexity. Table II summarizes the comparisons among the various Alamouti-coded multicarrier systems. Naturally, the strong points and the weak points of FBMC over the OFDM-based schemes remain intact in the proposed scheme over the Alamouti-coded versions of OFDM-based schemes.

Comparing the performance and complexity between FBMC and OFDM has been intensively and extensively established in the literature. Besides, it is cumbersome to provide the performance and complexity measures in numeric form for various combinations of the system parameters and channel models. Hence, referring to the analysis in the literature and based on the results in this paper, the relative comparisons in each measure are tabulated in Table II.

Note that in addition to the fundamental merits of FBMC such as excellent OOB suppression, no CP overhead or robustness against inter-user frequency/time synchronization, the proposed scheme achieves low PAPR which is inherited from LP-FBMC. On the other hand, it was shown in [34] that depending on the system configurations, FBMC modulation/demodulation requires about 3 to 7 times higher complexity than that of OFDM modulation/demodulation in terms of number of real multiplications (RMs) (see Table 2 in [34]). Consequently, except in terms of complexity, the proposed scheme is attractive over the other schemes in all aspects considered in Table II. As analyzed in Section V, high complexity of the proposed scheme is due to multiple candidate signal generation in TX side for PAPR reduction. For fair comparison, if we consider the case when Alamouti-coded CP-OFDM adopts the typical PAPR reduction schemes

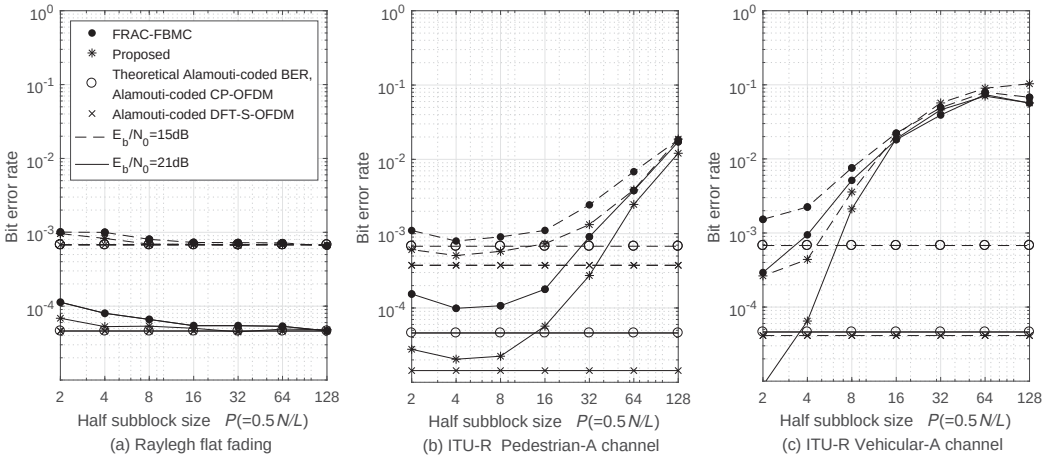

Fig. 12. BER comparisons among FRAC-FBMC [25], Alamouti-coded versions of CP-OFDM and DFT-S-OFDM and the proposed scheme, N=256, M=32, OQPSK.

TABLE II
OVERALL COMPARISON AMONG THE VARIOUS ALAMOUTI-CODED MULTICARRIER SYSTEMS

Alamouti-coded multicarrier scheme	Diversity order	PAPR	Out-of-band suppresion	Spectrum utilization	Complexity	Robustness against interuser synchronization errors
Alamouti-coded CP-OFDM	2	High	Poor	Overheads due to CP and guard subcarriers	Low	Needs larger CP and more guard subcarriers
Alamouti-coded DFT-S-OFDM	> 2	Low	Poor	Overheads due to CP and guard subcarriers	Low	Needs larger CP and more guard subcarriers
FRAC-FBMC	2	High	Excellent	Efficient due to no CP and good frequency localization	Moderate	Robust
Alamouti-coded LP-FBMC (Proposed)	> 2	Low	Excellent	Better than FRAC-FBMC due to no null in between half-subblocks	Moderate (single candidiate), High (eighit candidiates)	Robust

such PTS or SLM in order to catch up with low PAPR of the proposed scheme, its TX complexity is not low but rather comparable to that of the proposed scheme. This is because PTS or SLM for OFDM-based modulations requires quite large number of candidates (typically larger than 16), then the complexity for generating candidates extremely increases. Also in Alamouti-coded DFT-S-OFDM, in order to catch up with efficient spectrum utilization of the proposed scheme, higher order modulation with powerful channel coding should be employed and then, at the cost, the powerful channel coding should pay back large computation complexity for decoding in RX [34].

VIII. CONCLUSIONS

By using the proposed scheme, we tackled the two pending issues of FBMC, 1) Out of band (OOB) spectrum regrowth due to high power amplifier nonlinearity and 2) difficulty in combining multi-antenna technique with FBMC. These two issues are the main obstacles for adopting FBMC as the waveform for the next generation communication systems. We showed that the proposed scheme substantially ameliorates these two issues. For combining the multi-antenna technique with FBMC, we select the recently proposed ICI-free Alamouti code for FBMC as a target multi-antenna technique and then investigate whether the recently proposed PAPR reduction scheme (so called Low PAPR FBMC) is applicable to it. The analysis reveals that the merits of the two schemes, i.e., low PAPR and ICI free Alamouti coding remain intact. Considering the PAPR, BER, and data rate loss, each of which have been intensively investigated in this study, we conclude that the proposed scheme is a competitive solution for Alamouti-coded FBMC system in these three aspects.

REFERENCES

[1] T. Ihalainen, T. Hidalgo Stitz, M. Rinne, and M. Renfors, "Channel equalization in filter bank based multicarrier modulation for wireless communications," *EURASIP Journal on Applied Signal Processing*, Nov. 2006.
[2] J. Vihriala, N. Ermolova, E. Lahetkangas, O. Tirkkonen, and K. Pajukoski, "On the waveforms for 5G mobile broadband communications," in *Proc. 2015 IEEE 81st Vehicular Technology Conference (VTC Spring)*, May. 2015.
[3] S.S. Krishna Chaitanya Bulusu, H. Shaiek, and D. Roviras. "Prediction of spectral regrowth for FBMC-OQAM system using cumulants," in *Proc. 2014 IEEE 10th International Conference on Wireless and Mobile Computing, Networking and Communications (WiMob)*, pp. 402-406, Oct. 2014.
[4] D. Qu, S. Lu, and T. Jiang. "Multi-block joint optimization for the peak-to-average power ratio reduction of FBMC-OQAM signals," *IEEE Transactions on Signal Processing*, vol. 61, no. 7, pp. 1605-1613, Jan. 2013.
[5] C. Ye, Z. Li, T. Jiang, C. Ni, and Q. Qi, "PAPR reduction of OQAM-OFDM signals using segmental PTS scheme with low complexity," *IEEE Transactions on Broadcasting*,vol. 60, no. 1, pp. 141-147, Mar. 2013.
[6] G. Cheng, H. Li, B. Dong, and S. Li, "An improved selective mapping method for PAPR reduction in OFDM/OQAM system," *Communications and Network*, vol. 5 no.3 pp. 53-56, Sep. 2013.
[7] S. S. Krishna Chaitanya Bulusu, H. Shaiek, D. Roviras, and R. Zayani, "Reduction of PAPR for FBMC-OQAM systems using dispersive SLM technique," in *Proc. 2014 11th International Symposium on Wireless Communications Systems (ISWCS)*, pp. 26-29, Aug. 2014.

[8] A. Skrzypczak, P. Siohan, and J. P. Javaudin, "Reduction of the Peak-to-average Power Ratio for OFDM-OQAM Modulation," in *Proc. 63rd IEEE VTC*, pp. 2018-2022, May 2006.
[9] Y. Zhou, T. Jiang, C. Huang, and S. Cui, "Peak-to-average power ratio reduction for OFDM/OQAM signals via alternative-signal method," *IEEE Transactions on Vehicular Technology*, vol. 63, no. 1, pp. 494-499, Jul. 2014.
[10] S. Lu, D. Qu, and Y. He, "Sliding window tone reservation technique for the peak-to-average power ratio reduction of FBMC-OQAM signals," *IEEE Wireless Communications Letters*, vol. 1, no. 4, pp. 268-271, Jul. 2012.
[11] D. Na and K. Choi, "Low PAPR FBMC," *IEEE Trans. on Wireless Commun.*, vol. 17, no. 1, pp. 182-193, Jan. 2018.
[12] C. H. Yuen, P, Amini, and B. Farhang-Boroujeny, "Single carrier frequency division multiple access (SC-FDMA) for filter bank multicarrier communication systems," *2010 Proceedings of the Fifth International Conference on Cognitive Radio Oriented Wireless Networks and Communications*, Jun. 2010.
[13] T. Ihalainen, A. Viholainen, T. Stitz, M. Renfors, and M. Bellanger, "Filter bank based multi-mode multiple access scheme for wireless uplink," in *Proc. Signal Processing Conference(EUSIPCO)*, vol. 9, Glascow, Scotland, pp. 1354-1358, Aug. 2009.
[14] M. Bellanger, D. L. Ruyet, D. Roviras, and M. Terre, "FBMC physical layer: a primer," PHYDYAS, Jan. 2010.
[15] Chrislin Lele, Pierre Siohan and Rodolphe Legouable. "The alamouti scheme with CDMA-OFDM/OQAM," *EURASIP Journal on Advances in Signal Processing* 2010, pp. 1-13.
[16] Rostom Zakaria and Didier Le Ruyet, "A novel filter-bank multicarrier scheme to mitigate the intrinsic interference: application to MIMO systems," *IEEE Trans. on Wirel Commun.*, vol. 11 no. 3, March 2012, pp. 1112-1123.
[17] Rostom Zakaria and Didier Le Ruyet, "On interference cancellation in Alamouti coding scheme for filter bank based multicarrier systems," *ISWCS*, 2013. pp. 1-5.
[18] D. Kong, X. Xia, and T. Jiang, "An Alamouti coded CP-FBMC-MIMO system with two transmit antennas," Science China Information Sciences, vol. 58, no. 10, pp. 1-6, Oct. 2015.
[19] R. Zakaria and D. Le Ruyet, "A novel FBMC scheme for spatial multiplexing with maximum likelihood detection," in *Proc. 7th Int. Symp. Wireless Commun. Syst. (ISWCS)*, Sep. 2010, pp. 461-465.
[20] M. Caus and A. I. Perez-Neira, "Multi-stream transmission for highly frequency selective channels in MIMO-FBMC/OQAM systems," *IEEE Trans. Signal Process.*, vol. 62, no. 4, pp. 786-796, Feb. 2014
[21] A. I. Perez-Neira et al., "MIMO signal processing in offset-QAM based filter bank multicarrier systems," *IEEE Transactions on Signal Processing*, vol. 64, no. 21, pp. 5733-5762, Nov. 2016.
[22] Markku Renfors, et al., "A block-Alamouti scheme for filter bank based multicarrier transmission," *European Wireless Conference*, 2010, pp. 1031-1037.
[23] D. Na and K. Choi. "Intrinsic ICI-Free Alamouti Coded FBMC," *IEEE Commun. Lett.*, vol. 20, no. 10, pp. 1971-1974, Jul. 2016.
[24] J. Li, D. Chen, D. Qu, and T. Jiang, "Block-wise Alamouti schemes for OQAM-OFDM systems with complex orthogonality," Wireless Communications and Mobile Computing, vol. 16, no. 17, pp. 2975-2990, Dec. 2016.
[25] D. Na and K. Choi. "Generalization of the phase shift condition in Intrinsic ICI-free Alamouti-coded FBMC," *IEEE Commun. Lett.*, vol. 21, no. 8, pp. 1747-1750, Aug. 2017.
[26] Ciochina, Cristina, et al. "New PAPR-preserving mapping methods for single-carrier FDMA with space-frequency block codes." *IEEE Trans. on Wireless Commun.*, vol. 8, no. 8, 2009, pp. 5176-5186.
[27] D. Na, "Low PAPR FBMC," *MATLAB Central* Available: https://kr.mathworks.com/matlabcentral/fileexchange/66725-low-papr-fbmc
[28] M. Terre, "FBMC Modulation / Demodulation," *MATLAB Central* Available: https://www.mathworks.com/matlabcentral/fileexchange.
[29] H. S. Sourck, Y. Wu, Jan W. M. Bergmans, S. Sadri, B. F. Boroujeny, "Complexity and Performance Comparison of Filter Bank Multicarrier and OFDM in Uplink of Multicarrier Multiple Access Networks," IEEE Trans. Signal Process., vol. 59, no. 4, pp. 1907-1912, Apr. 2011.
[30] H. S. Sourck, S. Sadri, "Frequency-Domain Carrier Frequency and Symbol Timing Offsets Estimation for Offset QAM Filterank Multicarrier Systems in Uplink of Multiple Access Networks," Wireless Personal Communications., vol. 70, no. 2, pp. 601-615, May. 2013.
[31] D. Gregoratti, X. Mestre, "Uplink FBMC/OQAM-based Multiple Access Channel: Distortion Analysis under Strong Frequency selectivity," IEEE Trans. Signal Process., vol. 64, no. 16, pp. 4260-4272, Aug. 2016.
[32] J. Dore, N. Cassiau, D. Ktenas, "Low complexity frequency domain carrier frequency offset compensation for uplink multiuser FBMC receiver," 2014 EuCNC., Jun. 2014, no. 14543837.
[33] M. Hazewinkel, "Dirichlet kernel," in *Encyclopedia of Mathematics*, Rotterdam: The Netherlands: Springer, 2001.
[34] L.G. Baltar, F. Schaich, M. Renfors and J. A. Nossek, "Computational complexity analysis of advanced physical layers based on multicarrier modulation," in Future Network & Mobile Summit (FutureNetw), 2011. IEEE, 2011, pp. 1-8.
[35] ITU-R M.1225, "Guidelines for Evaluations of Radio Transmission Technologies for IMT-2000," 1997.
[36] Theodore S. Rappaport, et al., "Millimeter wave mobile communications for 5G cellular: It will work!," *IEEE Access*, May 2013, pp. 335-349.